Microsecond Carrier Lifetimes, Controlled p-Doping, and Enhanced Air Stability in Low-Bandgap Metal Halide Perovskites

Alan R. Bowman,[†] Matthew T. Klug,[‡] Tiarnan A. S. Doherty,[†] Michael D. Farrar,[‡] Satyaprasad P. Senanayak,[†] Bernard Wenger,[‡] Giorgio Divitini,[§] Edward P. Booker,[†] Zahra Andaji-Garmaroudi,[†] Stuart Macpherson,[†] Edoardo Ruggeri,[†] Henning Sirringhaus,[†] Henry J. Snaith,*[,‡] and Samuel D. Stranks*[,†]

[†]Cavendish Laboratory, Department of Physics, University of Cambridge, JJ Thomson Avenue, Cambridge CB3 0HE, United Kingdom

[‡]Clarendon Laboratory, Department of Physics, University of Oxford, Parks Road, Oxford OX1 3PU, United Kingdom

[§]Department of Materials Science and Metallurgy, University of Cambridge, 27 Charles Babbage Road, Cambridge CB3 0FS, United Kingdom

S *Supporting Information*

ABSTRACT: Mixed lead−tin halide perovskites have sufficiently low bandgaps (~1.2 eV) to be promising absorbers for perovskite−perovskite tandem solar cells. Previous reports on lead−tin perovskites have typically shown poor optoelectronic properties compared to neat lead counterparts: short photoluminescence lifetimes (<100 ns) and low photoluminescence quantum efficiencies (<1%). Here, we obtain films with carrier lifetimes exceeding 1 μs and, through addition of small quantities of zinc iodide to the precursor solutions, photoluminescence quantum efficiencies under solar illumination intensities of 2.5%. The zinc additives also substantially enhance the film stability in air, and we use cross-sectional chemical mapping to show that this enhanced stability is because of a reduction in tin-rich clusters. By fabricating field-effect transistors, we observe that the introduction of zinc results in controlled p-doping. Finally, we show that zinc additives also enhance power conversion efficiencies and the stability of solar cells. Our results demonstrate substantially improved low-bandgap perovskites for solar cells and versatile electronic applications.
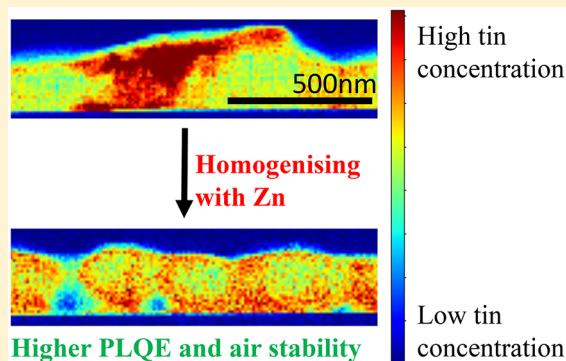
Metal halide perovskites based on methylammonium (MA) or formamidinium (FA) lead (Pb) halide derivatives show enormous promise as high-performance and inexpensive solar cells and light-emitting devices.[1] Advantages include tunable and direct bandgaps,[2] strong absorption,[3] long charge diffusion lengths[4] (when compared to film thickness), and high tolerance to defects.[5] State-of-the-art lead-based perovskite solar cells have bandgaps around 1.6 eV,[6] and record power conversion efficiencies (PCEs) in the laboratory are now above 25%.[7]

An exciting area for lead halide perovskites is tandem solar cell configurations, which provide a route for surpassing the single-junction Shockley−Queisser efficiency limit of ~33%.[8] In all tandem devices, a low-bandgap absorber (<1.3 eV) is required to achieve a notable efficiency gain.[9] While the first generation of commercial, perovskite-based tandem devices are likely to use silicon as the low-bandgap material,[10] there is an even greater

potential for adopting perovskites as both the high- and low-bandgap absorbers, for example, due to enhanced radiative recycling[11] and compatibility with deposition on lightweight, flexible substrates. To date, the highest-performing low-bandgap perovskites use mixtures of lead and tin, which exhibit bandgaps as low as 1.23 eV.[12] Single-junction PCEs for lead-tin-based devices are typically in the range of 17%,[13] with one recent report of 20%,[14] and have reached as high as 23.1% in a two-terminal tandem configuration with a wide-bandgap perovskite absorber.[14] These performances are still far below practical efficiency limits expected of 30 and 34% for single-junction and tandem perovskite configurations, respectively.[15−17] In addition,

there are stability issues owing to the sensitivity of Sn^{2+}, which can readily oxidize to Sn^{4+} in the presence of oxygen or moisture, leading to uncontrollable p-type doping[18] and eventual degradation of the perovskite structure. Although some control of this p-doping has been reported in the pure tin systems, such control has yet to be reported in the mixed lead−tin systems.[19]

One of the reasons for the relatively poor solar cell performance in low-bandgap mixed Pb−Sn perovskites films is that, in contrast to standard 1.6 eV perovskites, these Pb−Sn films have low reported photoluminescence quantum efficiencies (PLQEs), consistent with a large density of sub-bandgap trap states.[20] This large trap density has a negative impact on device performance, limiting the maximum achievable open-circuit voltage.[21] The PLQEs under solar illumination conditions in lead−tin alloys are reported to be on the order of 0.1% or lower[22] and photoluminescence (PL) lifetimes are generally on the order of a few nanoseconds, with three recent exceptions where lifetimes of 0.1−1.2 μs have been observed.[13,14,23] By comparison, well-passivated lead halide perovskite films have been reported to have PLQEs under solar illumination greater than 30%[24,25] and PL lifetimes as long as 8 μs.[26]

Here, we present FA-based Pb−Sn iodide thin-film perovskites with PLQEs up to 3.5%, PL lifetimes exceeding 1 μs, and enhanced stability against ambient air by employing ZnI_2 as an additive in the precursor solution. We perform transient absorption spectroscopy (TAS) and characterize electrical gating of the thin films to demonstrate that the Zn additives control the level of p-type doping in films. We demonstrate that these properties can translate to enhanced performance and short-term stability of thin solar cells with perovskite absorbers containing ZnI_2. Scanning transmission electron microscopy energy-dispersive X-ray spectroscopy (STEM-EDX) cross sections reveal that the processing with Zn leads to a more uniform mixing of Pb and Sn. This improved homogeneity reduces the density of Sn-rich regions that are otherwise the sites that lead to oxygen-induced degradation, leading to a greater tolerance to air exposure. X-ray diffraction (XRD) results hint that there may be some incorporation of Zn into the perovskite structure, providing a potential lever for controlled doping. These results represent an extremely promising step toward high-performance, stable, low-bandgap bottom cells for perovskite−perovskite tandems.

We fabricated thin films of $FAPb_{0.5}Sn_{0.5}I_3$-based perovskites by spin-coating a single precursor solution (main components FAI, SnI_2, and PbI_2, with the addition of 20% SnF_2 with respect to SnI_2 and 6% $Pb(SCN)_2$ with respect to PbI_2). For deposition, we used a gas quenching method[27,28] in a nitrogen-filled glovebox. In addition, we replaced a small quantity of the PbI_2/ SnI_2 precursor with ZnI_2, which has previously been shown to enhance lead-based perovskites.[29,30] Defining x to be the molar percentage of ZnI_2 relative to the number of moles of FAI in the precursor solution, we fabricated films with x = 0, 2, 5, and 10% (see SI Experimental Methods for further details). The resulting polycrystalline films have a uniform grain size, with a slightly smaller grain size for x = 5% but of the same order of magnitude (∼200 nm diameter; see SI Figure S1). We encapsulated all films inside of a nitrogen-filled glovebox directly after fabrication.

In Figure 1, we show PL measurements from pristine (x = 0%) and zinc-containing (x = 5%) films. We observe the position and shape of the PL peak to be similar for both films (Figure 1a, inset), but the fwhm gives a hint of differences, with the x = 5% peak being 10 meV narrower than the x = 0% peak. This small
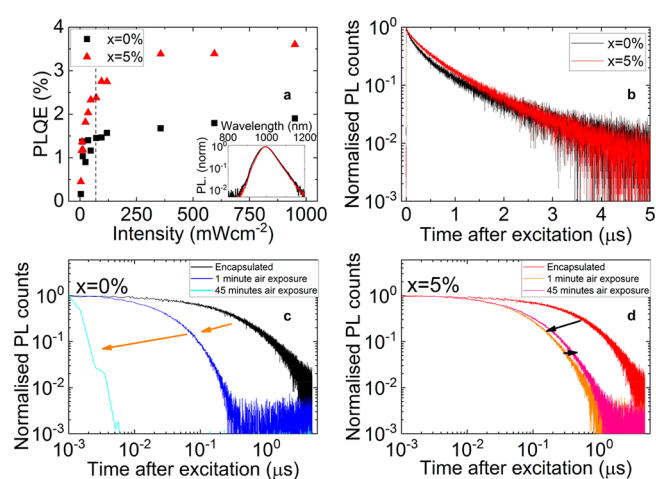

Figure 1. (a) PLQE with laser intensity when illuminated by a 648-nm continuous wave laser for x = 0 and 5% films. The dashed vertical line corresponds to 1 sun equivalent excitation density. The inset shows typical PL spectra. (b) Normalized PL decays for the same films, when illuminated by a 635-nm pulsed laser with intensity of 50 nJ cm^{-2}. PL decays of x = 0 and 5% films are shown in (c) and (d), respectively, recorded when samples are encapsulated (as in b), following 1 min of air exposure and after 45 min of air exposure.

reduction in fwhm is in line with a more homogeneous film composition, in agreement with our findings in the latter part of this work. We find that for both samples the PLQE increases with increased excitation density (Figure 1a), which we attribute to a trap-filling effect at higher carrier densities and an increasing competitiveness of radiative recombination with trap-assisted recombination, as is observed for the pure lead counterparts.[31,32] For x = 0%, the PLQE reaches 1.5% at excitation densities equivalent to those realized under solar operating conditions (1 sun; see SI Experimental Methods) and a maximum of 2.0% at higher densities (∼13 suns). These values increase further for x = 5%: at 1 sun, the PLQE is 2.5% and plateaus at 3.5% at ∼13 suns. Highly Sn rich perovskites have shown reasonable PLQE values of close to 1% due to the rapid radiative recombination of conduction band electrons with the sea of p-doped carriers.[33] However, for the more stable, lower-bandgap, technologically relevant compositions around the 50:50 Pb:Sn range, the highest previously reported PLQE values are ∼0.1%,[22,34] 1 order of magnitude lower than what we observe here. We note that we see a slight increase in root-mean-square roughness of the films from 24 ± 5 nm (x = 0%) to 36 ± 5 nm (x = 5%). This change in roughness will contribute to the increase in observed PLQE but is not the only contributing factor because the PL lifetime also increases. An increase in absolute PLQE is beneficial for properties such as the open-circuit voltage of solar cells. We can further exaggerate this effect by adjusting the deposition process (for instance, raising the height of the gas gun) and observing that the peak PLQE can increase to as high as 10%, which is primarily due to enhanced light outcoupling from increased density of pinholes (Figure S2). We observed that similar PLQE values can be obtained even after storage of encapsulated films in a nitrogen glovebox for 1 month (Figure S3).

Figure 1b shows time-resolved PL (TRPL) measurements employing time-correlated single-photon counting (TCSPC) (see Figure S4 for other compositions and for unnormalized decays). We reveal PL lifetimes (defined as the time taken to fall to $\frac{1}{e}$ of the initial value) of 0.36 μs for x = 0% and 0.49 μs for x =

5% at a fluence of 50 nJ cm^{-2}. We observe that the initial PL signal has a second-order dependence on laser power at this excitation density, suggesting that we are primarily observing the recombination of photoexcited electrons and holes in bimolecular processes (Figure S5). At lower fluences (5 nJ cm^{-2}), we observe lifetimes extending beyond 1 μs, reaching 1.5 μs for x = 0% and 1.19 μs for x = 5% (see Table S1 for all measured lifetimes). This fluence dependence highlights an interesting observation: at higher fluences (50 nJ cm^{-2}), the films processed with ZnI$_2$ have longer lifetimes, while at lower fluences (5 nJ cm^{-2}), pristine films have longer lifetimes. We explain these observations later by demonstrating that at lower fluences we move toward a regime more dominated by doping for the case of x = 5% films, where shorter lifetimes are expected (compared to films with less doping). This also explains the increase in PLQE at low excitation densities for x = 5% films.

We emphasize that the long lifetimes reported here were achieved only by encapsulating the films immediately after fabrication. If we stored films overnight even in a nominally clean nitrogen-filled glovebox before encapsulation, this resulted in lower PLQEs and PL lifetimes. The use of tin fluoride and lead thiocyanate additives also resulted in films with improved optoelectronic quality (Figure S6). Therefore, we attribute the high PLQEs and long lifetimes, even in the control samples, to rapid encapsulation and improved fabrication processing. These results were observed in multiple batches from different laboratories, suggesting that this fabrication method is highly reproducible.

To investigate the stability of films in ambient air, we removed the encapsulation and again measured PL lifetimes over a period of 45 min. Our results (Figures 1c,d and S7 for unnormalized decays) show that all films have a reduction in PL lifetime immediately following atmospheric exposure. The lifetime in zinc-containing films then remains comparatively stable, while the lifetime of x = 0% films drops substantially to ~1 ns after 45 min of air exposure. These results suggest that processing with ZnI$_2$ leads to enhanced resilience to degradation of optoelectronic properties in ambient air.

We performed TAS on encapsulated films to better understand the charge carrier decay kinetics, following methods described by Richter et al.[35] Here, we focused on the change of absorption between 800 and 1000 nm, which includes a broad ground-state bleach centered at 950 nm that appears after photoexcitation with a 532 nm pulsed laser (see Figure S8 for spectra). By integrating the TAS spectrum about the center of this ground-state bleach (±30 nm), we can monitor the decay of the ground-state bleach over several orders of magnitude in signal intensity. Because $\Delta T/T$ is small, the ground-state bleach is proportional to the number of photoexcited charges in the perovskite film, as exemplified by the linear relationship between early-time ground-state bleach recorded and laser power (see Figure S8 and SI Note 1). We scale our decay kinetics by the initial excitation density to obtain the number of excited charges following photoexcitation, $n(t)$ (see SI Note 2). We find that TA decays at different excitation densities overlap well, though we note some deviations from this overlap at the earliest times, which we attribute to charges slowly funneling down to the lowest-energy sites within films; we exclude these time windows from this analysis (see Figure S8 for further discussion).

In Figure 2a,b, we plot $n(t)$ versus $\frac{dn(t)}{dt}$ for x = 0 and 5%, respectively. Excitations in our films are observed to decay according to first-order, second-order, and third-order pro-
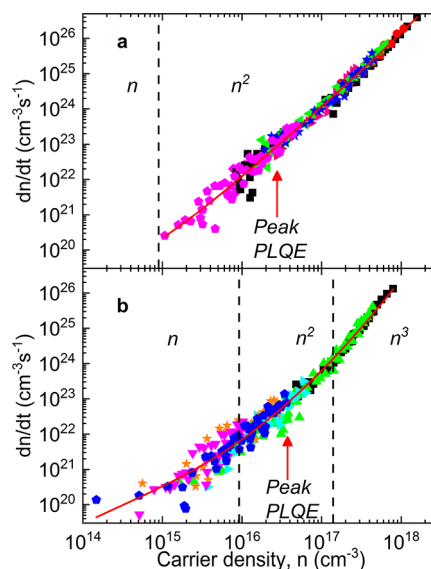

Figure 2. Carrier density, n, versus decay rate, $\left(\frac{dn}{dt}\right)$ for x = (a) 0 and (b) 5% films. Solid red lines show plots fitted with $\frac{dn}{dt} = -an - bn(n + p_0) - cn^3$. Dashed black lines are placed at $\frac{a}{b}$ and $\frac{b}{c}$ to highlight transitions between different decay regimes. Red arrow marks where the peak PLQE was obtained in Figure 1.

cesses. Low-bandgap lead—tin perovskites are p-type materials, meaning that in addition to bimolecular radiative recombination, first-order radiative recombination between an excited electron and a background hole can also play a role; $\frac{dn}{dt} = -an - bn(n + p_0) - cn^3$. Here, a is a nonradiative trapping term, b the second-order recombination rate, c an Auger recombination term, and p_0 the background hole concentration. We perform a logarithmic least-squares fit to our data to extract decay rates (see Table S2 for values). For x = 0%, the decay is dominated by bimolecular processes at nearly all excitation densities probed (for $10^{15}-10^{18}$ cm^{-3}). In contrast, we are able to observe regions where first-, second-, and third-order kinetics dominate for x = 5% films. Our results also show that the charge densities that yield the highest PLQE values correspond to bimolecular recombination in all films (Figure 2).

The excitation density at which first-order and second-order rate processes contribute equally to the decay of excitations ($an = bn^2$) is given by $n_{1-2} = \frac{a}{b}$. In our films, this critical carrier density is an order of magnitude higher for the x = 5% film ($n_{1-2} = 9.2 \times 10^{15}$ cm^{-3}) than that for the x = 0% film ($n_{1-2} = 0.9 \times 10^{15}$ cm^{-3}). We also note that at low excitation densities, PLQE $\approx \frac{bp_0}{a}$. From our measurements, the x = 5% films have a higher a value but also a higher PLQE (including at low excitation densities). We explain this by proposing that there is an increase in p-type doping (p_0) within our films with the addition of ZnI$_2$. This also explains the observation that the PL lifetime for x = 5% films increases less rapidly with decreasing fluence than that for x = 0% films.

In order to quantify the p-type doping, we use parameters from our TA data to fit the low-energy region of our PLQE measurements. This enables us to measure the background hole concentration (see SI Note 3, Table S2, and Figure S9). While for x = 0% we are only able to place an upper bound on p_0 (2.5 × 10^{14}cm^{-3}), for x = 5% we obtain a density of ~1 × 10^{15}cm^{-3}.

Thus, the background hole concentration is higher for $x = 5\%$ than the 0% analogue.

To confirm and explore the nature of doping induced by the ZnI_2 additive, we fabricated bottom gate/bottom contact perovskites field-effect transistors (FETs) using $x = 0$ and 5% perovskites films as the active layer. Surprisingly, both devices exhibited clean transistor characteristics at room temperature, with the expected p-type channel (Figure 3a,b). While there
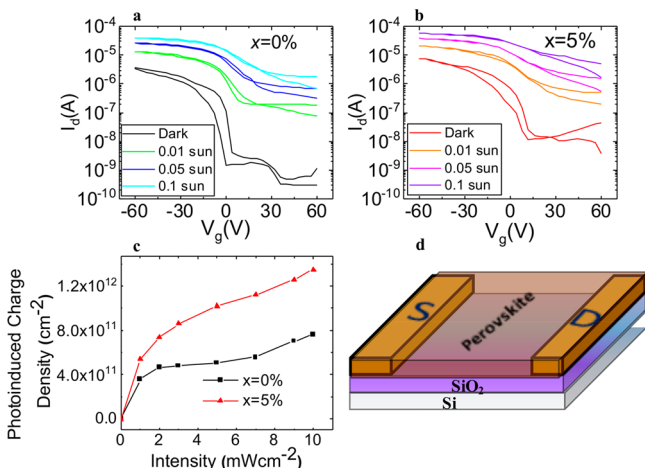

Figure 3. Electrically gated measurements of charge transport and photoinduced doping studies on a bottom contact/bottom gate FET device (channel length 100 μm, channel width 1 mm) fabricated with x = (a) 0 and (b) 5% perovskite layers. Photoinduced characteristics correspond to white light excitation densities across the range stated. (c) Estimated photoinduced charge carrier number density in perovskite thin-film FETs. (d) Schematic of the FET architecture.

have been some previous reports of transistors fabricated from $MAPbI_3$ and other neat lead- or neat tin-based perovskites,[36,37] to the best of our knowledge, this is the first report of a transistor based on low-bandgap mixed lead−tin perovskites. The observation of p-type transport is in agreement with previous transport characterization of Sn-based perovskites performed using terahertz conductivity[18] and Hall Effect measurements.[38] FET devices fabricated with the inclusion of Zn exhibit enhanced p-type behavior, with the channel current increasing approximately 3 times compared to $x = 0\%$ films. Furthermore, a positive turn-on voltage and larger off current for the $x = 5\%$ film both point toward enhanced p-type doping. The field-effect mobility (μ_{FET}) reaches a value of 0.007 cm^2/(V s) for $x = 5\%$ and 0.003 cm^2/(V s) for $x = 0\%$, with both values being comparable to previous lateral FET mobility measurements on perovskite thin films, where transport laterally across many grain boundaries in the FET device can significantly reduce effective mobilities recorded relative to single-crystal or terahertz measurements.[37] We note that control devices fabricated from ZnI_2-only solutions yielded insulating characteristics (Figure S10), demonstrating that the observed enhancements in mobility originate from the Zn additives in the perovskites rather than from the ZnI_2 ionic solid.

We illuminated our FET devices with white light to a maximum intensity of 10 mW/cm^2 ($\sim$0.1 sun equivalent) to investigate photodoping effects (Figure 3a,b). In both devices, we observed an enhancement in channel current, I_d, but the current still remained higher for $V_g < 0$, indicating that of the photogenerated charge carriers holes are more mobile than electrons. Photoinduced charge density in the perovskite FETs are shown in Figure 3c (see SI Experimental Methods for calculation details). The charge density is approximately 3 times higher for $x = 5\%$ films compared to that for $x = 0\%$ films, again pointing to reduction in trap density, which enables more charges to exist in the film under steady-state illumination. A
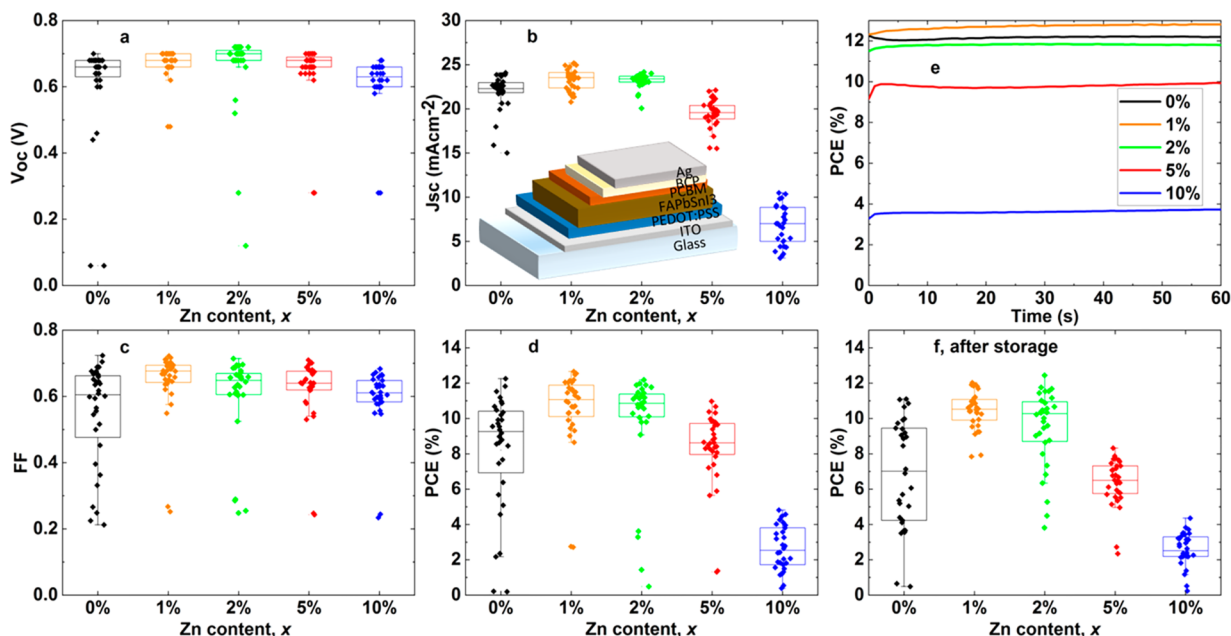

Figure 4. Box and whisker plots showing the thin solar cell (a) open-circuit voltage (V_{oc}), (b) short-circuit current (J_{sc}), (c) fill factor (FF), and (d) PCE, with $x = 0−10\%$. The inset in (b) is a schematic of the device stack used. (e) Champion pixel PCE of each composition held at the initial maximum power point voltage for 60 s. (f) PCE of devices from (d) after 2 days of storage in a nitrogen-filled glovebox and 2.5 h of air exposure.

reduction in trap density gives a possible explanation for enhanced p-type doping for $x = 5\%$ films.

To validate our spectroscopic results in full solar cell devices, we fabricated thin solar cells in the architecture indium tin oxide (ITO)/poly(3,4-ethylenedioxythiophene) polystyrenesulfonate (PEDOT:PSS)/perovskite/[6,6]-phenyl C61 butyric acid methyl ester (PCBM)/bathocuproine (BCP)/Ag (Figure 4b, inset), with the perovskite containing varying fractions of ZnI$_2$ in the precursor solution (see SI Experimental Methods). We used the same perovskite film thickness as that in the above spectroscopic measurements, meaning that we did not maximize the short-circuit current, and an otherwise identical recipe except with a "solvent quench" step optimized for devices instead of a "gas quench" (see SI Experimental Methods and Figure S11 for TRPL curves demonstrating similar trends following air exposure and Figure S12 for SEM images of the sample surfaces). We show device results for Zn content varying from 0 to 10% in Figure 4a–d. There is a clear increase in all solar cell parameters with the addition of ZnI$_2$, with $x = 1\%$ being the optimum for overall performance (further discussed below). We found the $x = 1\%$ exhibited a median PCE of 11.1% and interquartile range of 1.8% (champion PCE 12.7%), compared to $(9.3 \pm 3.5)\%$ for $x = 0\%$ (champion 12.3%). In particular, we saw an increase in the open-circuit voltage and short-circuit current, both of which are consistent with the enhanced luminescence and reduced impact of traps ascertained from spectroscopic measurements. We note that these absolute performances are respectable given that the active layer is only ~200 nm thick to match our spectroscopic measurements.

In Figure 4e, we show the PCE of the champion pixel from each composition held at the initial maximum power point voltage for 60 s. We note that, while there is typically a decrease in PCE during the initial time for $x = 0\%$ films, this "burn in" is positive for $x = 1$ and 2% cells. Furthermore, we exposed the devices to air (2.5 h) and stored them in a nitrogen glovebox for 48 h before retesting. The $x = 0\%$ devices substantially degraded during this time, while the $x = 1$ and 2% devices had mostly maintained their efficiency (Figure 4f; see Figure S13 for all results from these experiments). We note that the devices were measured unencapsulated, whereas our results on bare films above (cf. Figure 1c,d) showed substantial degradation for the $x = 0\%$ composition without encapsulation. Subsequent measurements show that the overlying device layers, in particular, the metal electrode, provide protection for the devices (SI Note 4 and Figure S14), and thus, the $x = 0\%$ devices were still measurable, albeit substantially reduced in performance with respect to their Zn counterparts. These results show that the addition of Zn improves both the performance and short-term stability of the resulting devices, in line with our spectroscopic results.

Finally, in order to determine the mechanism by which ZnI$_2$ addition leads to the enhanced properties of the Pb–Sn films and devices, we performed scanning transmission electron microscopy and energy-dispersive X-ray spectroscopy (STEM/EDX) on cross sections of films deposited on Si substrates. We minimized air exposure during this process and used a capping layer of spiro-OMeTAD to limit exposure to the electron and ion beam during sample preparation (see SI Experimental Methods for details).

Figure 5a–c shows the chemical spatial distribution of Pb, Sn, and Zn in the perovskite films, with $x = 0\%$ below and $x = 5\%$ above in each case. Pb appears to be relatively homogeneously distributed through both films, with no significant differences
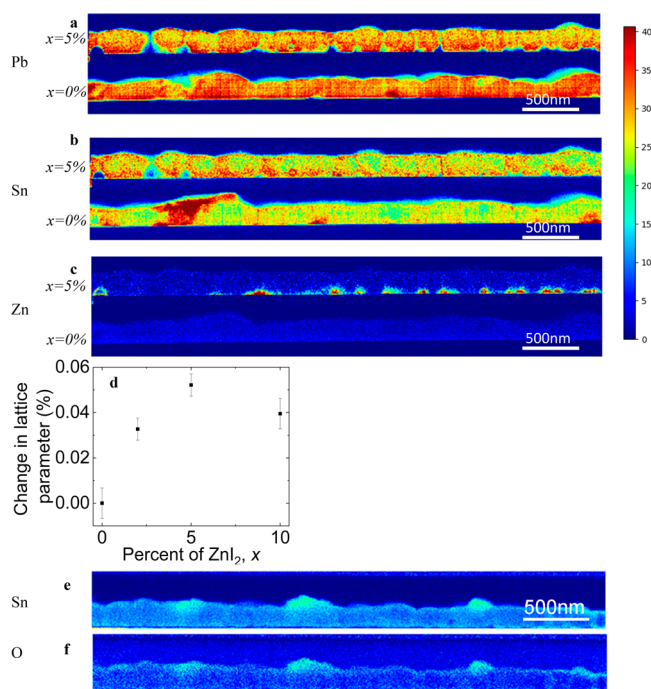

Figure 5. Distribution of (a) Pb, (b) Sn, and (c) Zn from a cross-sectional lamella as measured by STEM/EDX shown for films spun on silicon. In each figure, two films are shown; $x = 0\%$ is below, and $x = 5\%$ above. The color bar represents the signal intensity in arbitrary units. (d) XRD results showing an increase in lattice parameter with increasing fraction of ZnI$_2$ in the precursor solutions. (e) Cross section revealing Sn-rich regions on the surface of an $x = 0\%$ film, (f) with these same regions corresponding to increased concentration of oxygen with brief air exposure.

between the samples. However, the distribution of Sn is markedly different: for $x = 0\%$, we observe Sn-rich regions of size ~200 nm forming at the surface of the film, which are absent in the films prepared using ZnI$_2$ in the precursor solutions ($x = 5\%$). More generally, the Sn is much more uniformly intermixed with Pb in the Zn-containing samples. We observe that the majority of the added Zn localizes along the bottom of the film (substrate side); we show that this is not substrate-dependent by depositing films on the solar cell device contact PEDOT:PSS and obtaining the same results (Figure S15). The presence of this Zn layer may explain why our optimal device performance was found at $x = 1\%$ compared to $x = 5\%$ from spectroscopic measurements such as PLQE: there is a compromise between the beneficial effects from the addition of Zn such as doping and stability, and the excess Zn layer acting as an insulating layer limiting carrier collection.

XRD data (Figure 5d) reveals a small but statistically significant relative increase in perovskite lattice parameter (~0.05%) for the films with $x > 0\%$, consistent with a small quantity of Zn (<1%) being distributed throughout bulk of the $x = 5\%$ film (potentially at interstitial sites) but at a level below the detection limits of our STEM/EDX measurements (see Figure S16 for XRD spectra). We also note that the width of the XRD peaks was comparable for all compositions, and thus, we do not see any clear differences in grain size or strain effects.

We observe from further STEM/EDX measurements that oxygen in the film is primarily associated with the Sn-rich regions of the $x = 0\%$ films (Figure 5e,f). As has been proposed by Leitjens et al.,[39] the mechanism for low-bandgap perovskite degradation is the reaction of Sn with oxygen. Therefore, the

absence of these Sn-rich regions (as in the $x = 5\%$ films) renders greater resistance to degradation in ambient air.

Overall, our results show that films prepared with ZnI_2 in the precursor solutions exhibit more homogeneous mixing of Pb:Sn, higher PLQE and conductivity, a simultaneous increase in the p-doping, and a greater resistance to ambient air exposure. We propose that the ZnI_2 may both help during film formation and play an active role as a dopant either in interstitial or lattice sites, as was suggested by Saidaminov et al.[40] for larger-bandgap films. We speculate that the improved film formation could be due to the ZnI_2 seeding growth of higher-quality grains that are more chemically homogeneous, possibly due to the additives assisting the formation of more homogeneous perovskite complexes in the precursor solution. Further work will be required to confirm this mechanism.

We have demonstrated low-bandgap mixed lead—tin metal halide perovskite films with substantially better optoelectronic properties than those previously reported in the literature. We report carrier lifetimes over 1 μs in neat encapsulated films and PLQEs of 3.5% following the addition of zinc iodide to the precursor solution used to fabricate the films. The addition of zinc also dramatically increases the stability of the films to ambient air, with long PL lifetimes of films retained following air exposure. We further demonstrate that Zn additives can be used to control the p-type nature of the films, as is shown by clean transistor behavior; solar cells fabricated from these materials also show enhanced performance and short-term stability with Zn compared to the controls. We attribute these enhancements to improved mixing of Pb and Sn within the perovskite as well as possible trap management through Zn incorporation within the film. Our work demonstrates improved low-bandgap perovskite films and devices and highlights this material's potential in versatile electronic applications.

ASSOCIATED CONTENT

Ⓢ Supporting Information

The Supporting Information is available free of charge on the ACS Publications website at DOI: 10.1021/acsenergy-lett.9b01446.

> Methods, further supporting discussion, SEM images, further measurements of PLQE, TRPL, TAS, transistors, solar cell devices, XRD, and STEM-EDX(PDF)

AUTHOR INFORMATION

Corresponding Authors
*E-mail: sds65@cam.ac.uk.
*E-mail: henry.snaith@physics.ox.ac.uk.

ORCID Ⓘ
Bernard Wenger: 0000-0001-9026-7064
Giorgio Divitini: 0000-0003-2775-610X
Henry J. Snaith: 0000-0001-8511-790X
Samuel D. Stranks: 0000-0002-8303-7292

Author Contributions

Samples were prepared by M.T.K., S.P.S., M.D.F., and A.R.B. A.R.B. performed and analyzed PLQE, TCSPC, and TAS measurements. PLQE was performed in conjunction with E.R. and S.M. and TCSPC with assistance from B.W. Transistor fabrication and measurements were performed by S.P.S. Solar cell fabrication and measurements were carried out by M.D.F. STEM/EDX measurements were carried out by T.A.S.D. and G.D. SEM measurements were performed by T.A.S.D., Z.A.-G.,

and M.D.F. XRD was performed by E.P.B. with analysis being carried out by E.P.B. and A.R.B. S.D.S. supervised the project and supervised E.R., S.M., T.A.S.D. and A.R.B. H.S. supervised work done by S.P.S. H.J.S. supervised M.T.K. and M.D.F. H.S. supervised S.P.S. A.R.B. and S.D.S. wrote the manuscript with contributions from other authors.

Notes

■ REFERENCES

(1) Green, M. A.; Ho-Baillie, A.; Snaith, H. J. The Emergence of Perovskite Solar Cells. *Nat. Photonics* **2014**, *8* (7), 506−514.
(2) Zhang, W.; Eperon, G. E.; Snaith, H. J. Metal Halide Perovskites for Energy Applications. *Nat. Energy* **2016**, *1* (6), 16048.
(3) Frost, J. M.; Butler, K. T.; Brivio, F.; Hendon, C. H.; van Schilfgaarde, M.; Walsh, A. Atomistic Origins of High-Performance in Hybrid Halide Perovskite Solar Cells. *Nano Lett.* **2014**, *14*, 2584−2590.
(4) Wehrenfennig, C.; Liu, M.; Snaith, H. J.; Johnston, M. B.; Herz, L. M. Charge-Carrier Dynamics in Vapour-Deposited Films of the Organolead Halide Perovskite CH3NH3PbI3−xClx. *Energy Environ. Sci.* **2014**, *7* (7), 2269−2275.
(5) Hutter, E. M.; Gélvez-Rueda, M. C.; Osherov, A.; Bulović, V.; Grozema, F. C.; Stranks, S. D.; Savenije, T. J. Direct−Indirect Character of the Bandgap in Methylammonium Lead Iodide Perovskite. *Nat. Mater.* **2017**, *16*, 115−120.
(6) Saliba, M.; Matsui, T.; Seo, J.-Y.; Domanski, K.; Correa-Baena, J.-P.; Nazeeruddin, M. K.; Zakeeruddin, S. M.; Tress, W.; Abate, A.; Hagfeldt, A.; et al. Cesium-Containing Triple Cation Perovskite Solar Cells: Improved Stability, Reproducibility and High Efficiency. *Energy Environ. Sci.* **2016**, *9* (6), 1989−1997.
(7) *NREL Best Research-Cell Efficiencies.* https://www.nrel.gov/pv/assets/pdfs/best-research-cell-efficiencies.20190802.pdf (2019).
(8) Shockley, W.; Queisser, H. J. Detailed Balance Limit of Efficiency of P-n Junction Solar Cells. *J. Appl. Phys.* **1961**, *32* (3), 510−519.
(9) Vos, A. De Detailed Balance Limit of the Efficiency of Tandem Solar Cells. *J. Phys. D: Appl. Phys.* **1980**, *13* (5), 839−846.

(10) Futscher, M.; Ehrler, B. Efficiency Limit of Perovskite/Si Tandem Solar Cells. *ACS* **2016**, *1*, 863−868.

(11) Parrott, J. E. Radiative Recombination and Photon Recycling in Photovoltaic Solar Cells. *Sol. Energy Mater. Sol. Cells* **1993**, *30* (3), 221−231.

(12) Prasanna, R.; Gold-Parker, A.; Leijtens, T.; Conings, B.; Babayigit, A.; Boyen, H. G.; Toney, M. F.; McGehee, M. D. Band Gap Tuning via Lattice Contraction and Octahedral Tilting in Perovskite Materials for Photovoltaics. *J. Am. Chem. Soc.* **2017**, *139* (32), 11117−11124.

(13) Zhao, D.; Yu, Y.; Wang, C.; Liao, W.; Shrestha, N.; Grice, C. R.; Cimaroli, A. J.; Guan, L.; Ellingson, R. J.; Zhu, K.; et al. Low-Bandgap Mixed Tin−Lead Iodide Perovskite Absorbers with Long Carrier Lifetimes for All-Perovskite Tandem Solar Cells. *Nat. Energy* **2017**, *2* (4), 17018.

(14) Tong, J.; Tong, J.; Song, Z.; Kim, D. H.; Chen, X.; Chen, C.; Palmstrom, A. F.; Ndione, P. F.; Reese, M. O.; Dunfield, S. P. Carrier Lifetimes of > 1 μs in Sn-Pb Perovskites Enable Efficient All-Perovskite Tandem Solar Cells. *Science* **2019**, *364*, 475−479.

(15) Pazos-Outón, L. M.; Xiao, T. P.; Yablonovitch, E. Fundamental Efficiency Limit of Lead Iodide Perovskite Solar Cells. *J. Phys. Chem. Lett.* **2018**, *9*, 1703−1711.

(16) Hörantner, M. T.; Snaith, H. Predicting and Optimising the Energy Yield of Perovskite-on-Silicon Tandem Solar Cells under Real World Conditions. *Energy Environ. Sci.* **2017**, *10*, 1983−1993.

(17) Hörantner, M. T.; Leijtens, T.; Ziffer, M. E.; Eperon, G. E.; Christoforo, M. G.; McGehee, M. D.; Snaith, H. J. The Potential of Multijunction Perovskite Solar Cells. *ACS Energy Lett.* **2017**, *2* (10), 2506−2513.

(18) Noel, N. K.; Stranks, S. D.; Abate, A.; Wehrenfennig, C.; Guarnera, S.; Haghighirad, A.-A.; Sadhanala, A.; Eperon, G. E.; Pathak, S. K.; Johnston, M. B.; et al. Lead-Free Organic-Inorganic Tin Halide Perovskites for Photovoltaic Applications. *Energy Environ. Sci.* **2014**, *7*, 3061−3068.

(19) Milot, R. L.; Klug, M. T.; Davies, C. L.; Wang, Z.; Kraus, H.; Snaith, H. J.; Johnston, M. B.; Herz, L. M. The Effects of Doping Density and Temperature on the Optoelectronic Properties of Formamidinium Tin Triiodide Thin Films. *Adv. Mater.* **2018**, *30*, 1804506.

(20) Stranks, S. D. Nonradiative Losses in Metal Halide Perovskites. *ACS Energy Lett.* **2017**, *2* (7), 1515−1525.

(21) Rau, U. Reciprocity Relation between Photovoltaic Quantum Efficiency and Electroluminescent Emission of Solar Cells. *Phys. Rev. B: Condens. Matter Mater. Phys.* **2007**, *76* (8), 1−8.

(22) Zhao, B.; Abdi-Jalebi, M.; Tabachnyk, M.; Glass, H.; Kamboj, V. S.; Nie, W. A.; Pearson, J.; Puttisong, Y.; Godel, K. C.; Beere, H. E.; et al. High Open-Circuit Voltages in Tin-Rich Low-Bandgap Perovskite-Based Planar Heterojunction Photovoltaics. *Adv. Mater.* **2017**, *29*, 1604744.

(23) Leijtens, T.; Prasanna, R.; Bush, K. A.; Eperon, G.; Raiford, J. A.; Gold-Parker, A.; Wolf, E. J.; Swifter, S. A.; Boyd, C. C.; Wang, H.-P.; et al. Tin-Lead Halide Perovskites with Improved Thermal and Air Stability for Efficient All-Perovskite Tandem Solar Cells. *Sustain. Energy Fuels* **2018**, *2*, 2450−2459.

(24) Abdi-Jalebi, M.; Andaji-Garmaroudi, Z.; Cacovich, S.; Stavrakas, C.; Philippe, B.; Richter, J. M.; Alsari, M.; Booker, E. P.; Hutter, E. M.; Pearson, A. J.; et al. Maximizing and Stabilizing Luminescence from Halide Perovskites with Potassium Passivation. *Nature* **2018**, *555* (7697), 497−501.

(25) Braly, I. L.; Dequilettes, D. W.; Pazos-Outón, L. M.; Burke, S.; Ziffer, M. E.; Ginger, D. S.; Hillhouse, H. W. Hybrid Perovskite Films Approaching the Radiative Limit with over 90% Photoluminescence Quantum Efficiency. *Nat. Photonics* **2018**, *12* (6), 355−361.

(26) Dequilettes, D. W.; Koch, S.; Burke, S.; Paranji, R. K.; Shropshire, A. J.; Ziffer, M. E.; Ginger, D. S. Photoluminescence Lifetimes Exceeding 8 Ms and Quantum Yields Exceeding 30% in Hybrid Perovskite Thin Films by Ligand Passivation. *ACS Energy Lett.* **2016**, *1* (2), 438−444.

(27) Babayigit, A.; D'Haen, J.; Boyen, H. G.; Conings, B. Gas Quenching for Perovskite Thin Film Deposition. *Joule* **2018**, *2*, 1205.

(28) Conings, B.; Babayigit, A.; Klug, M. T.; Bai, S.; Gauquelin, N.; Sakai, N.; Wang, J. T. W.; Verbeeck, J.; Boyen, H. G.; Snaith, H. J. A Universal Deposition Protocol for Planar Heterojunction Solar Cells with High Efficiency Based on Hybrid Lead Halide Perovskite Families. *Adv. Mater.* **2016**, *28* (48), 10701−10709.

(29) Muscarella, L. A.; Petrova, D.; Jorge Cervasio, R.; Farawar, A.; Lugier, O.; McLure, C.; Slaman, M. J.; Wang, J.; Ehrler, B.; Von Hauff, E.; et al. Air-Stable and Oriented Mixed Lead Halide Perovskite (FA/MA) by the One-Step Deposition Method Using Zinc Iodide and an Alkylammonium Additive. *ACS Appl. Mater. Interfaces* **2019**, *11*, 17555−17562.

(30) Kooijman; Muscarella; Williams. Perovskite Thin Film Materials Stabilized and Enhanced by Zinc(II) Doping. *Appl. Sci.* **2019**, *9* (8), 1678.

(31) Deschler, F.; Price, M.; Pathak, S.; Klintberg, L. E.; Jarausch, D. D.; Higler, R.; Hüttner, S.; Leijtens, T.; Stranks, S. D.; Snaith, H. J.; et al. High Photoluminescence Efficiency and Optically Pumped Lasing in Solution-Processed Mixed Halide Perovskite Semiconductors. *J. Phys. Chem. Lett.* **2014**, *5*, 1421−1426.

(32) Stranks, S. D.; Burlakov, V. M.; Leijtens, T.; Ball, J. M.; Goriely, A.; Snaith, H. J. Recombination Kinetics in Organic-Inorganic Perovskites: Excitons, Free Charge, and Subgap States. *Phys. Rev. Appl.* **2014**, *2* (3), 1−8.

(33) Parrott, E. S.; Green, T.; Milot, R. L.; Johnston, M. B.; Snaith, H. J.; Herz, L. M. Interplay of Structural and Optoelectronic Properties in Formamidinium Mixed Tin−Lead Triiodide Perovskites. *Adv. Funct. Mater.* **2018**, *28*, 1802803.

(34) Konstantakou, M.; Stergiopoulos, T. A Critical Review on Tin Halide Perovskite Solar Cells. *J. Mater. Chem. A* **2017**, *5* (23), 11518−11549.

(35) Richter, J. M.; Abdi-Jalebi, M.; Sadhanala, A.; Tabachnyk, M.; Rivett, J. P. H.; Pazos-Outón, L. M.; Gödel, K. C.; Price, M.; Deschler, F.; Friend, R. H. Enhancing Photoluminescence Yields in Lead Halide Perovskites by Photon Recycling and Light Out-Coupling. *Nat. Commun.* **2016**, *7*, 13941.

(36) Lin, Y. H.; Pattanasattayavong, P.; Anthopoulos, T. D. Metal-Halide Perovskite Transistors for Printed Electronics: Challenges and Opportunities. *Adv. Mater.* **2017**, *29*, 1702838.

(37) Senanayak, S. P.; Yang, B.; Thomas, T. H.; Giesbrecht, N.; Huang, W.; Gann, E.; Nair, B.; Goedel, K.; Guha, S.; Moya, X.; et al. Understanding Charge Transport in Lead Iodide Perovskite Thin-Film Field-Effect Transistors. *Sci. Adv.* **2017**, *3*, e1601935−1.

(38) Stoumpos, C. C.; Malliakas, C. D.; Kanatzidis, M. G. Semiconducting Tin and Lead Iodide Perovskites with Organic Cations: Phase Transitions, High Mobilities, and near-Infrared Photoluminescent Properties. *Inorg. Chem.* **2013**, *52* (15), 9019−9038.

(39) Leijtens, T.; Prasanna, R.; Gold-Parker, A.; Toney, M. F.; McGehee, M. D. Mechanism of Tin Oxidation and Stabilization by Lead Substitution in Tin Halide Perovskites. *ACS Energy Lett.* **2017**, *2* (9), 2159−2165.

(40) Saidaminov, M. I.; Kim, J.; Jain, A.; Quintero-Bermudez, R.; Tan, H.; Long, G.; Tan, F.; Johnston, A.; Zhao, Y.; Voznyy, O.; et al. Suppression of Atomic Vacancies via Incorporation of Isovalent Small Ions to Increase the Stability of Halide Perovskite Solar Cells in Ambient Air. *Nat. Energy* **2018**, *3*, 648.